Optical Damage Limit of Efficient Spintronic THz Emitters

Sandeep Kumar, Anand Nivedan, Arvind Singh, Yogesh Kumar, Purnima Malhotra, Marc Tondusson, Eric Freysz, Sunil Kumar

Graphical abstract

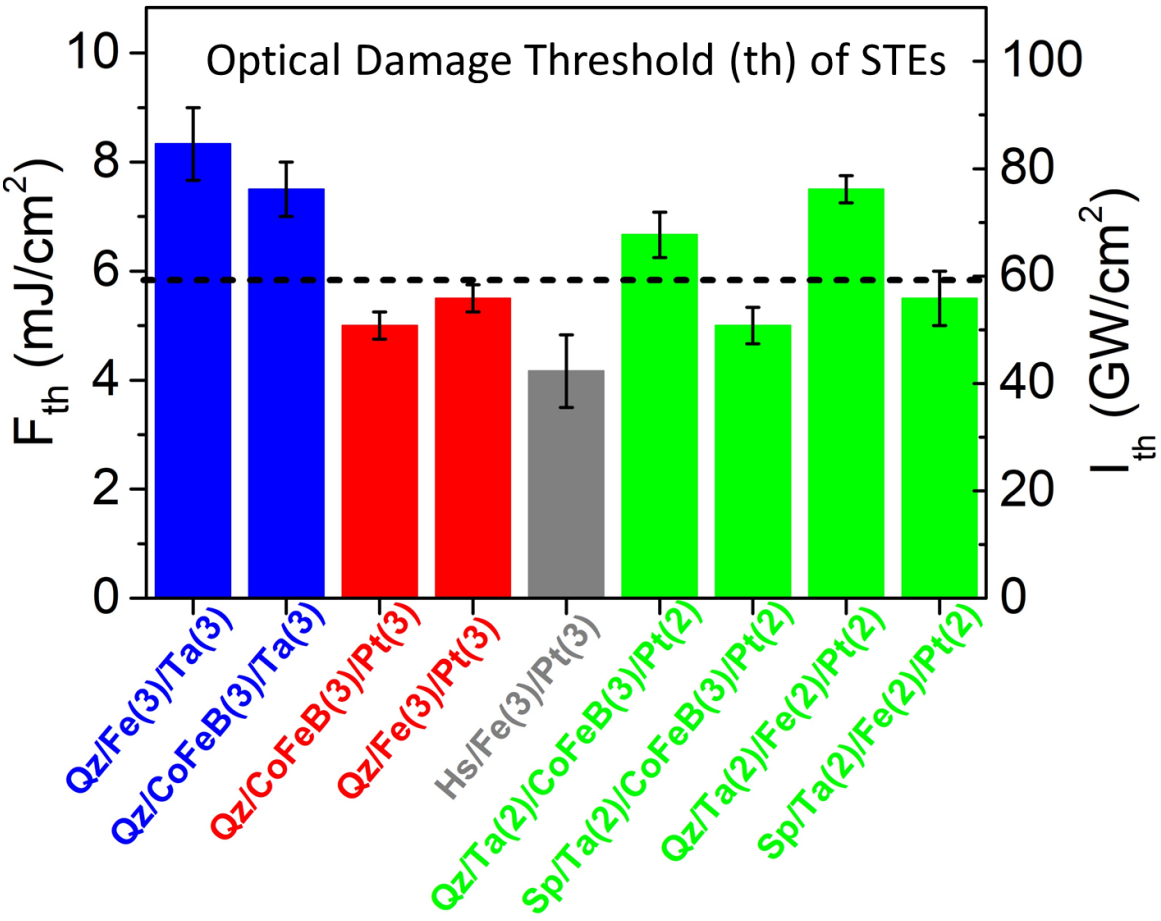

Highlights

- THz generation efficiency of (CoFeB,Fe)/(Pt,Ta) spintronic film heterostructures.
- Determination of optical damage threshold at NIR excitation.
- Mean value of the optical damage threshold is ~50 GW/cm^2.

Optical Damage Limit of Efficient Spintronic THz Emitters

Sandeep Kumar[1], Anand Nivedan[1], Arvind Singh[1], Yogesh Kumar[2], Purnima Malhotra[2], Marc Tondusson[3], Eric Freysz[3], and Sunil Kumar[1,#,*]

[1]Femtosecond Spectroscopy and Nonlinear Photonics Laboratory, Department of Physics, Indian Institute of Technology Delhi, New Delhi 110016, India

[2]Laser Science and Technology Center, Metcalfe House, Civil Lines, New Delhi 110054, India

[3]Univ. Bordeaux, CNRS, LOMA, UMR 5798, 33405 Talence, France

[#]Lead contact

*Corresponding Author: kumarsunil@physics.iitd.ac.in

SUMMARY

THz pulses are generated from femtosecond pulse-excited ferromagnetic/nonmagnetic spintronic heterostructures via inverse spin Hall effect. The highest possible THz signal strength from spintronic THz emitters is limited by the optical damage threshold of the corresponding heterostructures at the excitation wavelength. For the thickness-optimized spintronic heterostructure, the THz generation efficiency does not saturate with the excitation fluence even up till the damage threshold. Bilayer (Fe, CoFeB)/(Pt, Ta) based FM/NM spintronic heterostructures have been studied for an optimized performance for THz generation when pumped by sub-50 fs amplified laser pulses at 800 nm. Among them, CoFeB/Pt is the best combination for an efficient THz source. The optimized FM/NM spintronic heterostructure having α-phase Ta as the nonmagnetic layer, shows the highest damage threshold as compared to those with Pt, irrespective of their generation efficiency. The damage threshold of the Fe/Ta heterostructure on a quartz substrate is ~85 GW/cm^2.

INTRODUCTION

When ferromagnetic/nonmagnetic (FM/NM) metallic thin film heterostructures are irradiated with optical femtosecond laser pulses, emission of THz pulses takes place.(Li *et al.*, 2019; Wu *et al.*, 2017; Seifert *et al.*, 2017b; Seifert *et al.*, 2017a; Yang *et al.*, 2016; Seifert *et al.*, 2016; Kampfrath *et al.*, 2013a) Such emitters are unique in the sense that they combine the excitements from the three most active research fields, currently, the ultrafast lasers, spintronics, and THz radiation. The most commonly known process responsible for the THz pulse generation from FM/NM type spintronic heterostructures is the inverse spin Hall effect (ISHE).(Li *et al.*, 2019; Wu *et al.*, 2017; Seifert *et al.*, 2017b; Seifert *et al.*, 2017a; Yang *et al.*, 2016; Seifert *et al.*, 2016; Kampfrath *et al.*, 2013a) Beaurepaire *et al.*, for the first time in 2004, observed emission of THz radiation from femtosecond laser-excited ferromagnetic (Ni) thin film, where, it was suggested that femtosecond laser-induced ultrafast demagnetization process was responsible for the THz pulse emission.(Beaurepaire *et al.*, 1996) From the subsequent studies(Hilton *et al.*, 2004) it was realized that only weak THz radiation is possible from such a process. The role of the ultrafast demagnetization process for THz generation from single-layer FM films was further investigated with respect to the thickness of the film to find an optimal efficiency for a specific thickness.(Kumar *et al.*, 2015) Zhang and coworkers attributed anomalous Hall effect for the generation of THz radiation from thin single ferromagnetic, $(Fe_xMn_{1-x})_yPt_{1-y}$ layers.(Zhang *et al.*, 2019) Similarly, a few other studies in the literature have indicated the generation of a very weak THz radiation from femtosecond laser-excited NM metal-based structures.(Kadlec *et al.*, 2004) The issue of low efficiency was quickly resolved as soon as FM/NM-based metallic heterostructures were experimented upon using the femtosecond laser excitation,(Kampfrath *et al.*, 2013a) where, the ISHE was considered to be the underlying mechanism.(Saitoh *et al.*, 2006) Specifically, the ultrafast laser pulse induced nonequilibrium quenching of magnetization occurs in the ferromagnetic layer. Consequently, the formation of superdiffusive spin current takes place because of the higher mobility and lifetime of hot majority spins(Battiato *et al.*, 2012, 2010; Melnikov *et al.*, 2011). In the NM layer, strong spin-orbit coupling converts the spin current into transient charge current, which emits THz radiation. Not only a high generation efficiency but also broad bandwidth of the generated THz radiation became realizable.(Seifert *et al.*, 2016) Here, the spin Hall angle in the NM heavy metal layer, the spin polarization in the FM layer, the individual film quality, and thicknesses in the heterostructure, are the major contributing material parameters. In principle, the bandwidth of the THz radiation generated from these sources is limited by the duration of the excitation pulse only.(Seifert *et al.*, 2016)

THz generation from the above-mentioned spintronic heterostructures shows a nonsaturating behavior, i.e., nearly linearly increasing THz power with respect to the excitation power.(Torosyan *et al.*, 2018; Seifert *et al.*,

2018; Seifert *et al.*, 2017a; Seifert *et al.*, 2016; Wu *et al.*, 2017) By using proper thicknesses and combinations of the FM/NM layers in their heterostructures, and the optical conditions in the experiments, THz electric field strengths of a few hundreds of kV/cm along with broad bandwidth are achievable.(Seifert *et al.*, 2017a) Conventionally, high power THz radiation is generated from amplified laser pulse-excited nonlinear crystals such as lithium niobate,(Fülöp *et al.*, 2010) organic materials,(Hauri *et al.*, 2011), and the dual-color air plasma.(Bartel *et al.*, 2005; Kress *et al.*, 2004; Kumar *et al.*, 2021b; Kumar *et al.*, 2021c) For the realization of high-power THz radiation from air plasma, it requires very high-energy pump pulses. Nonlinear optical materials like lithium niobate crystal and organic crystals, which can sustain hard pumping and provide intense THz pulses, have limitations in terms of strict phase-matching conditions, absorption at THz frequencies, etc.(Fülöp *et al.*, 2020) The THz radiation with its electric field strength as high as a few MV/cm, is also possible these days.(Oh *et al.*, 2014) In principle, the efficiency of any solid-state material-based THz source is limited ultimately by the associated optical damage threshold.

The spintronic THz sources, very often, have been tested with low pulse energy femtosecond lasers for achieving broad bandwidth.(Torosyan *et al.*, 2018; Seifert *et al.*, 2016) In a very few cases, they have also been tested with the amplified laser pulses,(Seifert *et al.*, 2017a) for achieving high power THz radiation. Beyond a certain value of the excitation power, spin accumulation in the NM layer contributes to a weak saturating behavior.(Yang *et al.*, 2016; Kampfrath *et al.*, 2013a) Furthermore, like the nonlinear crystals, spintronic THz sources can be used only before their optical damage threshold. As compared to others, spintronic-based THz emitters have a large scope in terms of the choice of the materials that can be used, better tunability in polarization, bandwidth, and power. Optimization through excitation wavelength, sample geometry, applied magnetic field, etc., can be achieved easily.(Torosyan *et al.*, 2018; Seifert *et al.*, 2018; Seifert *et al.*, 2017a; Seifert *et al.*, 2016; Wu *et al.*, 2017; Herapath *et al.*, 2019; Kong *et al.*, 2019; Chen *et al.*, 2019; Feng *et al.*, 2018; Kumar *et al.*, 2021a) In the current study, we have experimentally determined the optical damage threshold of many popular spintronic THz emitters on different substrates by using femtosecond amplified laser pulses at 800 nm, which has not been reported explicitly in the literature, hitherto. Fe and CoFeB have been used for the FM layer and Pt and Ta (in α-phase) have been used as the NM layer in the bilayer spintronic heterostructures. These heterostructures have been tested for optimal THz power generation by using various combinations of the FM and NM layer thicknesses. Ultrafast demagnetization and inverse spin Hall effect have been invoked for the THz generation mechanism. Ta in its specific α-phase has been used in our heterostructures, in which, its role as a buffer layer and an efficient ISHE material has been determined. For Fe/Ta bilayer heterostructure on quartz substrate, the optical damage threshold is the highest at ~85 GW/cm^2, which is quite

comparable with that of the popularly used lithium niobate crystal. The THz generation efficiency of the thickness optimized Fe/Pt bilayer structure is found to be even better than the dual-color air plasma-based THz source for excitation pump energy levels below ~0.5 mJ. While, the CoFeB/Pt is a more efficient source than Fe/Pt, being consistent with the literature, we find it to be opposite in the case with Ta as the NM layer, i.e., THz power generation efficiency of Fe/Ta is much higher than that of the CoFeB/Ta. Differences found in the optical damage threshold of a particular heterostructure on different substrates are consistent with the differences in their THz generation efficiency. The reason has primarily to do with the optical power absorbed by them, a weak absorber has lower THz generation efficiency at any given excitation power, and also it has a higher damage threshold.

RESULTS AND DISCUSSION

All the results discussed through Figures 1 to 5 have been obtained at a fixed excitation pulse energy (average power) of ~0.35 mJ (350 mW) or the fluence of ~1.2 mJ/cm^2. Figure 1 summarizes the outcomes on the THz generation efficiency from various thickness combinations in the bilayer FM/NM heterostructures on quartz substrates that are fabricated by magnetron sputtering in ultrahigh vacuum (see the Experimental Section). FM layer is of either Fe or CoFeB and the NM layer is of either Pt or Ta, thereby allowing four possible FM/NM combinations for experimentation on them. The Ta layer is grown in its α-phase (see Supplementary Section S1). These results in Figure 1 provide the optimized thicknesses and their combinations for the total thickness of the bilayer structure such that maximum THz power is produced from them under the same conditions with the optical excitation, room temperature and humidity, optical alignment, and the detection by electro-optic sampling. A schematic of the THz pulse generation following excitation by a femtosecond laser pulse at near-infrared (NIR), is shown in Figure 1(A). A representative THz time-domain signal, E(t), and its Fourier spectrum, E(ω), are presented in Figure 1(B) and 1(C), respectively, generated from Fe(3)/Pt(2) bilayer heterostructure. All the THz generation and detection measurements reported in this paper have been done under room temperature and humidity (~50%) conditions that are realistic for all practical purposes, mainly, the applications in stand-off detection and screening. Hence, the strong far IR absorption lines due to the characteristic water absorption bands(Xin *et al.*, 2006) in the THz spectrum can be seen from Figure 1(C). The limited THz bandwidth (~0.2-5 THz) is mainly due to the ZnTe crystal used in our electro-optic sampling setup for THz pulse detection. The magnitude of the THz time-domain signal can be improved immensely if the enclosure of the experimental setup is purged with dry air. The enhancement factor may vary depending on the available bandwidth of the generated THz radiation. However, for consistency, all the results below have been obtained without any purging.

The femtosecond pump excitation (z-direction) of the FM layer, which is kept magnetized by B_{ext} along -y-direction, produces a spin current. The spin current, J_s in the z-direction gets injected into the NM layer of the heterostructure. Due to strong spin-orbit coupling in the NM layer by virtue of the ISHE,(Saitoh *et al.*, 2006) a charge current, J_c is produced in the x-direction as shown in Figure 1(A). Note that the magnetization direction is defined by the external magnetic field, B_{ext}, which is kept just above the saturation magnetization field of the FM layer. Briefly, the THz pulse generation process through ISHE in the FM/NM bilayer spintronic heterostructure is described here. NIR femtosecond excitation pulse stimulates the electrons in the FM metal layer from states below the Fermi level to above it, creating a non-equilibrium hot electron distribution.(Battiato *et al.*, 2010) The FM metal is such that there is a difference in its spin-up and spin-down electron densities and their transport properties in the respective bands.(Knorren *et al.*, 2000) This difference helps in producing a spin-polarized

current (J_s) to be injected into the NM layer employing a superdiffusive process if an appropriate thickness of the FM layer is used.(Battiato *et al.*, 2010; Melnikov *et al.*, 2011) Since the NM layer of the spintronics heterostructure is a heavy metal with high intrinsic spin-orbit coupling, opposite polarity spins are deflected in opposite directions by an amount proportional to the spin-Hall angle (γ) and hence produce a charge current density,(Hoffmann, 2013) given by the following relation.(Kampfrath *et al.*, 2013a; Wu *et al.*, 2017)

$$\overrightarrow{J_c} = \gamma.(\overrightarrow{J_s} \times \hat{m}) \quad (1)$$

Here, $\hat{m} = \vec{M}/|\vec{M}|$ is the magnetization direction. Therefore, the in-plane transient charge current J_c in the NM layer generates a pulse of THz radiation which has been measured by electro-optic sampling in our experiments.

Figures 1(D) to 1(I) show the results obtained from Fe/Pt structures on quartz substrate for different thicknesses of the two individual layers in nanometers (nm) as mentioned inside small parentheses. The raw THz signals obtained for fixed Fe thickness and varying Pt thickness are shown in Figures 1(D) and 1(E). Similarly, raw results for fixed Pt layer thickness and varying Fe layer thickness, are presented in Figures 1(F) and 1(G). For clarity, the consecutive time-domain traces in Figures 1(D-G) have been shifted vertically by a constant amount. As can be seen from Figures 1(H) and 1(I) that the root mean squared amplitude of the THz field ($E(t)_{RMS}$) is dependent on the thickness of the individual layers, there is an optimum value of the thickness where maximum THz power is generated. It is clear from the thickness-thickness color intensity plot in Figure 1(I) that the optimum thickness of the Fe layer is ~2 nm, that of the Pt layer is ~3 nm and for other values of thicknesses of the two layers, the maximum THz generation is found to be for thickness ~5 nm of the combined structure. These results are consistent with the literature.(Torosyan *et al.*, 2018) Therefore, for referral purposes later on in the manuscript, the optimized Fe/Pt heterostructure on quartz contains a 2 nm thick Fe layer and a 3 nm thick Pt layer. The optimum thickness of the Fe layer is very close to its critical thickness (~1.5 nm) for the change in the direction of the magnetic easy axis in the layer (please see the Supplementary Section S1). Determination of the thickness-dependent performance for THz emission was necessary because the optical damage threshold measurements are conducted on the thickness-optimized heterostructures.

Various parameters such as spin current generation in the FM layer, spin to charge current conversion and spin accumulation in the NM layer, optical and THz absorption in the total thickness, etc., contribute to the overall THz generation efficiency of the bilayer FM/NM heterostructures.(Papaioannou and Beigang, 2021) From Figure 1(H), it can be seen that for a fixed thickness of the Fe layer, there is an optimum thickness of the Pt layer at which maximum THz generation can be obtained. Efficient conversion of the spin-polarized current into the transient charge current in the NM layer is necessary for maximum THz generation efficiency(Haney *et al.*,

2013). The decrease in the THz signal at lower thicknesses is due to the limited spin decay length in the NM material. The optimum thickness of the Pt layer for generation of the highest THz signal from the heterostructure is about 3 nm, which is just above the spin decay length of ~1 nm in Pt.(Torosyan *et al.*, 2018; Seifert *et al.*, 2017b; Seifert *et al.*, 2016) A dramatic change in the THz RMS amplitude takes place with the thickness of the Fe layer changing from 2 nm to 1 nm in Figure 1(H). This is attributed to the change in magnetization easy axis going from being in-plane to out-of-plane, below a certain thickness (see the Supplementary Section S1). From Figures 1(H) and 1(I), it is clear that the optimum thickness of the Fe layer is about 2 nm. Similarly, it can be seen from the Figure that at smaller thicknesses of the Pt layer, the THz power continues to grow with the increasing thickness up till its optimum value at ~3nm. At the optimum thickness of the Fe layer, the decrease in the THz generation efficiency with the increasing Pt layer thickness (beyond 3 nm) can be understood in terms of a compromise between the spin to charge current conversion for the fixed excitation fluence and the overall THz attenuation in the bilayer heterostructure(Seifert *et al.*, 2016). The former is due to the spread of absorbed excitation power over a larger thickness in thick films. The overall thickness beyond which the THz generation efficiency starts to decrease is ~5nm.

The raw THz results for fixed thicknesses of Pt or Ta layer at 3 nm while the varying thickness of FM CoFeB layer from 2 to 5 nm in the CoFeB/Pt and CoFeB/Ta bilayers are presented in Figures 1(J) and 1(K), respectively. The RMS values of the THz signal for each sample are presented in Figure 1(L). It can be seen that the optimum value of the CoFeB layer thickness is close to 3 nm beyond which there is not much improvement in the THz generation efficiency and also the THz attenuation in the CoFeB does not increase much with its thickness up to 5 nm. In these cases, we have already used the optimum thickness of the Pt layer of ~3 nm. Our results (Figure 2) indicate that the optimum thickness of the Ta layer in the heterostructures is more than 5 nm, while almost no THz signal is measured from the bilayers containing Ta layer thickness below 2 nm. In addition to the opposite polarity THz signal, we also find much lower THz generation efficiency of the CoFeB/Ta than the CoFeB/Pt bilayers (Figures 1(J,K)). Both of these effects can be attributed to the opposite sign and much smaller spin-Hall angle, respectively, in the α-phase Ta as compared to Pt.(Kumar *et al.*, 2018; Sinova *et al.*, 2015)

The ultrafast demagnetization is also a process, which, under femtosecond excitation of FM layers, generates THz radiation and has been reported in several studies.(Beaurepaire *et al.*, 2004; Kumar *et al.*, 2015; Huang *et al.*, 2020) From our results presented in Figure 2(A), we intend to disseminate a conclusion that the FM and NM layers individually contribute very weakly to the THz generation process. As discussed later, in comparison, the THz signal produced by ISHE is about two orders of magnitude stronger from the bilayer heterostructures. From Figure 2(A), we can see that no THz signal is produced at all from Ta(5), Fe(2)/Ta(1.8), and CoFeB(3)/Ta(1.8)

samples. Clearly, the THz generation is not substantially enough either through ultrafast demagnetization in thin FM layers or through ISHE in FM/NM bilayers without having an appropriately thick NM layer. A weak THz generation from thick FM layers through ultrafast demagnetization is evident from our results also as presented in Figure 2(A) for the Fe(20)/Ta(1) and CoFeB(20)/Ta(1) samples, where the signals have been magnified by a factor of 10 for better visualization. These results are consistent with the literature.(Huang *et al.*, 2020) Here, in all of these cases, a very thin Ta layer has been utilized as a capping layer (thickness of ~1nm) for the FM film. For such a thin Ta layer, it does not contribute as the NM layer in the otherwise FM/NM heterostructures of Figure 2(B) also having no THz signal from Fe(2)/Ta(1.8). Furthermore, almost no role of the external magnetic field can be noted in Figure 2(A) for the weak THz signal generation from FM films.(Huang *et al.*, 2020; Huang *et al.*, 2019)

THz generation by ISHE in thin-film Fe/Ta heterostructures can be observed only if the Ta layer thickness is larger than 2 nm. The corresponding results have been presented in Figure 2(B), where, data is shown for Fe layer thicknesses 2 nm and 3 nm, while Ta layer thickness varying from 1.8 nm to 5 nm. These results again confirm that the optimized thickness of the Fe layer for maximum THz signal is ~2 nm. As shown in the inset of Figure 2(B), the THz signal continues to grow with the increasing Ta layer thickness. While comparing the results for the Fe/Pt (Figure 1) and Fe/Ta (Figure 2(B)), we find that the optimum thickness of the α-phase Ta layer is much larger than the Pt layer. It is noteworthy to note from the results discussed above that the demarcation line for the thickness of the α–phase Ta layer below which it can be used as a capping or buffer layer is ~2nm. However, it may vary depending on the different phases of the Ta.(Kumar *et al.*, 2018) Besides the fact that the spin Hall angle in Ta (all phases) is opposite in sign to that in the conventionally used Pt layer, depending on the phase, its spin Hall angle and resistivity both span over a large range(Kim *et al.*, 2015; Bansal *et al.*, 2017; Kumar *et al.*, 2018; Niimi and Otani, 2015). The THz generation efficiency through the ISHE is directly proportional to the spin Hall angle, spin-mixing conductance, and spin diffusion length, while it is inversely proportional to the resistivity of the material layer.(Dang *et al.*, 2020; Seifert *et al.*, 2016) All these parameters need to be optimized so as to constitute a correct figure of merit of the most efficient spintronic THz emitter. Ta in β-phase has a higher value of spin Hall angle (~ -0.15) (ref. (Liu *et al.*, 2012)) than Pt (~0.12) (ref. (Obstbaum *et al.*, 2014)). However, due to high resistivity in this phase, it is not a good substitute for the highly expensive Pt layer. Owing to the reduced charge current generation following optical pumping, the conversion efficiency into THz radiation is highly limited in the high resistive β-phase of Ta(Seifert *et al.*, 2016).

The presence of an interface and intermixing at the interface can contribute to the generation of THz signal through various mechanisms, which can be probed through excitation pulse helicity-dependent measurements.

For example, the THz generation process based on ISHE does not depend on helicity, whereas, the spin-dependent photogalvanic effect (SDPE) is dependent on the helicity of the excitation pulse.(Li *et al.*, 2019) Our experimental results presented in Figure 3 suggest that only ISHE is responsible for the THz generation from FM/NM heterostructures. Here in Figure 3, the results have been presented for optimized Fe(2)/Pt(3) bilayer for linearly polarized (LP), elliptically polarized (EP), left circularly polarized (LCP), and right circularly polarized (RCP) excitation light. Therefore, the contribution from the SDPE into the THz pulse generation from FM/NM bilayers is negligibly small. We may also point out that a recent report on the THz pulse generation from optically excited antiferromagnetic/nonmagnetic film heterostructure arises due to a different mechanism, where, helicity-dependent outcomes can be possible.(Qiu *et al.*, 2020)

As per Eq. (1) for the ISHE being responsible for the THz pulse generation, the magnetization of the FM layer can be used as a control to manipulate the amplitude and polarization of the emitted THz radiation.(Qiu *et al.*, 2018; Torosyan *et al.*, 2018) In Figures 4(A) and 4(B), we have shown the time-domain THz electric field signals from Fe(2)/Pt(3) and Fe(2)/Ta(3) samples, respectively, recorded with and without the external field, B_{ext}. For the Fe layer, the saturation magnetic field (coercive field) is ~50 Oe as confirmed from the in-plane M-H measurements (see Supplementary Section S1). Therefore, for the magnetic field effect, we have shown the results for three values of B_{ext}, i.e., 0B (no field), 1B ~200 Oe, and 2B ~400 Oe. In the first case (0B), only the effect of any remanence field is observed in terms of a small magnitude THz signal,(Kampfrath *et al.*, 2013a) due to the pinned magnetic domains that could avoid reorientation after removal of the external field. For the other two field values (1B and 2B), the THz signal is already saturated. Except for the change in the magnitude, the temporal profiles of the THz pulses are exactly the same irrespective of the external magnetic field value (see inset of Figure 4(A)). As shown in the inset of Figure 4(B), the polarity of the generated THz signal can be reversed by flipping the direction of the external magnetic field as per the ISHE in Eq. (1).(Seifert *et al.*, 2016)

Now in Figure 5, we compare the THz generation efficiency of the near thickness optimized Fe/Pt, Fe/Ta, CoFeB/Pt, and CoFeB/Ta bilayer heterostructures having the same thicknesses of the FM and NM layers in each of the combinations and under the same experimental conditions. The CoFeB(3)/Pt(3) heterostructure provides ~40% stronger THz emission than that from Fe(3)/Pt(3). The enhanced THz signal from the prior can be attributed to the larger spin injection into the NM layer and is consistent with the literature.(Seifert *et al.*, 2016) Interestingly, the case is entirely reversed for the Fe/Ta and CoFeB/Ta bilayers, which contain Ta as the NM layer. Another highlight from Figure 5(A) is that for the same α-phase Ta as the NM layer in the heterostructures, the THz signal from Fe(3)/Ta(3) is stronger by ~300% than that in CoFeB(3)/Ta(3). This observation indicates that the spin injection efficiency in the CoFeB(3)/Ta(3) might have got severely affected by the seemingly larger

crystalline mismatch and roughness at the FM/NM interface, both of which essentially affect the spin mixing conductance ($g_{\uparrow\downarrow}$) and the spin-Hall angle at the interface.(Dang *et al.*, 2020)

The spin mixing conductance, $g_{\uparrow\downarrow}$ is a measure of the spin current injected from the FM layer into the NM layer. Assuming a simple precession motion, the spin current density is related to the spin mixing conductance through a relation given by(Kumar *et al.*, 2018; Mosendz *et al.*, 2010): $J_s = (1/2\pi)e\omega \mathrm{Re}(g_{\uparrow\downarrow})\sin(\theta_c)$, where, $e, \omega, \mathrm{Re}(g_{\uparrow\downarrow}),$ and θ_c are the electronic charge, the angular frequency of spin dynamics, the real part of spin mixing conductance, and the magnetization precession angle, respectively. Therefore, a higher value of $\mathrm{Re}(g_{\uparrow\downarrow})$ ensures an enhanced THz emission through Eq. (1). The values of the spin mixing conductance reported in the literature are: ~3.5-6×10^{19} m^{-2} for CoFeB/Pt,(Zhu *et al.*, 2019; Conca *et al.*, 2017; Kim *et al.*, 2014) ~3-5×10^{19} m^{-2} for Fe/Pt,(Conca *et al.*, 2016; Papaioannou *et al.*, 2013) and ~0.7-1.4×10^{19} m^{-2} for CoFeB/Ta.(Conca *et al.*, 2017; Kim *et al.*, 2014) For the CoFeB/Ta case in refs. (Conca *et al.*, 2017; Kim *et al.*, 2014), Ta in its β-phase was used(Conca *et al.*, 2017; Kim *et al.*, 2014). Similar values for Fe/Ta could not be found in the literature. Moreover, the FM/NM spintronic heterostructures containing α-phase Ta have not been studied much in the literature. The α-phase of Ta is more metallic than the β-phase and hence can be better suited for the THz applications though it has comparatively a slightly smaller spin-Hall coefficient(Kumar *et al.*, 2018). The experimentally observed small relative change in the THz signal from CoFeB/Pt as compared to Fe/Pt (Figure 5(A)) seems consistent with the corresponding values of the $g_{\uparrow\downarrow}$. However, the much larger THz signal from Fe/Ta than the CoFeB/Ta demands that the corresponding $g_{\uparrow\downarrow}$ value in Fe/Ta should be higher than the CoFeB/Ta. Our THz experiments suggest a higher value of $g_{\uparrow\downarrow}$ for the Fe/Ta as compared to CoFeB/Ta. The conclusion from the results in this part is that Pt should be favored with CoFeB, while α-phase Ta should be favored with Fe in their FM/NM bilayer heterostructures for best THz generation performance.

Besides the electronic mechanisms,(Saitoh *et al.*, 2006) a comparison in the magnitude of the THz signals from two FM/NM combinations can be used to quantify the spin-Hall angle in a given NM layer(Seifert *et al.*, 2018). For example, the THz generation efficiencies of CoFeB/Pt and CoFeB/W were compared to determine the spin-Hall angle in W to be γ ~ -0.056, which was very close to its exact value.(Mondal *et al.*, 2017) We have used the known value of γ = 0.12 in Pt(Seki *et al.*, 2008; Sinova *et al.*, 2015; Obstbaum *et al.*, 2014) to estimate the same in α-phase Ta by comparing the THz signal strengths from Fe/Pt and Fe/Ta in Figure 5(B), where the same thickness FM layer is used. From the ratio between the RMS values of the corresponding THz signal strengths in Figure 5(B), γ_{Ta} ~ -0.047 has been estimated. Of course, for the exact determination of the γ value in α-phase Ta, one needs information about the corresponding $g_{\uparrow\downarrow}$ value and other material parameters,

precisely(Seifert *et al.*, 2018). Nevertheless, our estimated value of γ_{Ta} ~ -0.047 here closely matches with the value from the literature(Kumar *et al.*, 2018), where spin-torque ferromagnetic resonance study on α-phase Ta containing NiFe/Ta structure was carried out.

For a quantitative assessment of the THz generation efficiency of the above spintronic emitters, here, we compare the THz signal strengths with a more standard high-power THz source, i.e., the dual-color air plasma source. To do so, excitation fluence-dependent measurements were carried out on both types of sources using configurations I and II of the experimental setup as shown in Figures S2.1 and S2.2, respectively, of the Supplementary Information. In Figure 6(A), a comparison between the THz signals from the thickness optimized Fe(2)/Pt(3) spintronic heterostructure on quartz substrate and the dual-color air-plasma sources is shown. Here, an excitation pulse energy of ~0.35 mJ was used for both types of sources. It can be seen that the THz emission from both sources is quite comparable. In fact, the THz generation efficiency of the spintronic source is slightly better than the air-plasma source at low excitation pulse energies as shown in Figure 6(B), where, the excitation pulse energy-dependence has been shown in a large range. It may be noted that the magnitude of the THz radiation from the spintronic source is underestimated from its actual value because of the fact that the optical gating beam size, the position of the nonlinear crystal for detection, and the optical alignment in the two configurations (I and II) are kept unchanged (see Section S2 in the Supplementary Information).

In the absence of a THz power/energy meter, we could estimate the strength of the generated THz signal from our measurements in the units of THz electric field (kV/cm). To do so, we have compared in Figure 6(B), the excitation energy-dependent THz signal strengths in nA (lock-in units) from the air plasma source (our experiments) with the values in units of kV/cm reported in the literature for the same source(Bartel *et al.*, 2005). We point out that these experiments have been performed under very similar experimental conditions with the excitation pulse duration, the SHG crystal, focusing, etc. Nearly one-to-one correspondence in the two units can be seen in Figure 6(B) for the air-plasma source. Therefore, a THz signal of strength 10 nA in our case can be considered equal to the actual THz field strength of ~170 kV/cm (see Section S5 in the Supplementary Information). Furthermore, the peak amplitude of the THz electric field from the air-plasma source linearly increases with the excitation pulse energy in Fig. 6(B). The linear behavior is a good indication that the electro-optic effect in the ZnTe electro-optic crystal is still in the linear regime for the detection of such intense THz pulses.(Gallot and Grischkowsky, 1999) This is because of the excitation energy values being much above the air-plasma ionization threshold value(Augst *et al.*, 1991; Bartel *et al.*, 2005) of ~10^{14} W/cm^2. A slight difference in the two graphs in Figure 6(B) can be attributed to the differences in the experimental conditions due to room temperature, humidity, and the optical arrangements in the experimental setup.

As mentioned before, for reasonable excitation pulse energy, the spintronic source produces a slightly higher THz signal than the air-plasma source (Figure 6(A)) and it grows nearly linearly with the excitation pulse energy. However, at very high values of the excitation pulse energy, the spintronic sources will not work because of the optical damage to the material. Here, we come to the second main point of our paper, i.e., to determine the optical damage threshold of various spintronic THz emitters, which were thickness optimized in our study. In this case of the spintronic emitters only, the results and discussion are provided in terms of excitation fluence (mJ/cm^2) or peak intensity (GW/cm^2). The latter is simply the pulse-energy/pulse duration per unit area. The excitation fluence was varied in a large range by using a neutral density filter in the excitation path while keeping the excitation beam size fixed at ~1 mm on the sample. These measurements were done in a different configuration of the experimental setup as shown in Figure S3 of the Supplementary Information. In this case, the spintronic source was placed at the focal point between the two inner parabolic mirrors, and a converging optical beam through the hole of one of the parabolic mirrors irradiated the sample. For the Fe(2)/Pt(3) heterostructure on the quartz substrate, the THz peak amplitude with respect to the excitation fluence has been presented in Figure 7(A). The magnitude of the THz signal continues to grow with the excitation fluence upto ~5.5 mJ/cm^2, beyond which a sudden decrease in the THz signal can be noticed. This is due to the optical damage of the spintronic material at a certain optical damage threshold value. Optical microscopy images of the sample, before and after the optical damage are shown in the inset of Figure 7(A) (please see the Supplementary Information S4 for more details).

Before the optical damage starts, only a weak saturation behavior of the THz signal with the excitation fluence can be seen in Figure 7(A). The irradiation time at each excitation fluence was about 5 minutes. The saturation can arise due to two reasons mainly, the spin accumulation and the local heating.(Kampfrath *et al.*, 2013b; Huisman *et al.*, 2016) If the spin accumulation induced saturation(Kampfrath *et al.*, 2013a; Yang *et al.*, 2016) was stronger than the latter, we should have observed saturation in the THz signal quite early in the data shown in Figure 7(A). The contrasting result, therefore, suggests that the local heating-induced saturation in the THz signal is more dominant. Our observation that the THz generation from the spintronic emitters has not saturated before reaching the optical damage threshold is quite interesting. Circumventing the limitation of the optical damage will, therefore, help unlock the full potential of the spintronic THz emitters.

The optical damage threshold (ODT) of the spintronic emitters depends on the FM/NM layer combinations in the bilayer and trilayer heterostructures, their material types, and the underlying substrates. To investigate this aspect in somewhat detail, we have carried out experiments on multiple samples and on different substrates. Particularly, the ODT values have been determined for the spintronic heterostructures having optimized

thicknesses of the FM and NM layers that were found out earlier in the paper. The corresponding results and the ODT values for each in mJ/cm^2 (excitation or pump fluence) and GW/cm^2 (peak intensity) are presented in Figure 7(B). More details of the experiments are given in Section S4 of the Supplementary Information. In Figure 7(B), the samples have been named as per the substrates and the bi- or the tri-layer heterostructures used in them. The numbers inside small parentheses in the names of the samples represent the thickness of the individual layer in nm. The substrates used are: 1 mm thick quartz (Qz) plate, 1 mm thick sapphire (Sp) plate, 0.38 mm thick highly resistive silicon wafer (Hs). The mean value of the ODT fluence for the spintronic THz emitters under the current study is about 5.8 mJ/cm^2 and the corresponding ODT peak intensity is ~60 GW/cm^2. This value is only a few times smaller than the value (~100 GW/cm^2) for the popular lithium niobate crystal, which has been used routinely as a high-power THz source in the literature.(Meng *et al.*, 2016; Fülöp *et al.*, 2020)

From Figure 7(B), we notice that the bilayer heterostructures with Ta as the NM layer on the quartz substrate show the highest ODT fluence value of ~8.34 mJ/cm^2 (peak intensity ~85 GW/cm^2). Therefore, quartz is suggested to be a good substrate for better heat sink management to achieve higher ODT in the spintronic THz emitters. It appears from Figure 7(B) that the ODT value is nearly independent of the type of the FM layer but affected by the type of the NM layer in the bilayer heterostructures on the same type of substrate. The reason for this fact is related to the overall absorptance of the sample. To substantiate this fact, we measured the fluence-dependent reflectance (R) and transmittance (T) values of the samples at various incident angles. One set of those results for the substrate corrected R and T values at different pump-fluences, is presented in Figure 8 for the representative samples of CoFeB(3)/Pt(3) and CoFeB(3)/Ta(3) bilayers on the quartz substrate. More details can be found in the Supplementary Information part. In Figure 8, solid symbols are the data points taken at increasing the fluences while the open symbols are at lowering the fluences. The optical microscopy images were taken after the optical damage of the CoFeB/Pt sample at certain fluences (powers) indicated by vertically up arrows. There was a very weak damage to the CoFeB/Ta sample upto the highest experimental fluence as compared to CoFeB/Pt. Thin continuous and dotted black lines in Figures 8(A) and 8(B) are the absorptance (A = 1 - R - T) values while increasing and decreasing the excitation fluences, respectively. After the damage, while lowering the fluence values, there is no change in the R, T, and A values as can be seen from Figure 8. At any excitation fluence, the transmittance (absorptance) of CoFeB(3)/Pt(3) is smaller (higher) than that of the CoFeB(3)/Ta(3). Obviously, for the excitation wavelength of 800 nm, the lower value of absorptance of CoFeB(3)/Ta(3) than CoFeB(3)/Pt(3) is consistent with the higher damage threshold value for the prior.

In comparison to the spintronic heterostructures on the quartz substrate, those on sapphire and HR silicon substrates show the least ODT values. This is to do with the higher optical absorption at 800 nm and less heat dissipation in those substrates. It is known that the metal-dielectric interface in spintronic THz emitters significantly improves the THz emission efficiency because of the enhanced optical absorption in such structures.(Feng *et al.*, 2018) Although a few nanometer thick dielectric layer is almost non-dissipative for THz, it will also lead to a quicker heat deposition in the sample to cause an early optical damage of the sample. For example, as shown in Figure 7(B), the optical damage threshold of the sample on SiO_2/Si substrate is lower than that of the same on a quartz substrate. The presence of a few nm thick oxide layer hinders the transfer of heat to the more thermally conducting silicon substrate, thereby, justifying the lower ODT value in this case. In our study, among the three substrates viz HR-silicon/SiO_2, quartz, and sapphire, quartz acts as the most efficient heat sink and hence provides the highest damage threshold to the thickness optimized efficient spintronic heterostructures studied in the first part of the paper.

CONCLUSION

In conclusion, optical damage threshold of various spintronic heterostructures as efficient THz emitters has been evaluated in this paper. Such a study is very important from the point of view that in recent literature on the spintronic THz emitters, they have been suggested to be the highly efficient, powerful, and broadband sources. The inverse spin-Hall effect is the main origin for high power THz generation from the bi- and tri-layer FM/NM type spintronic THz emitters. Detailed experiments were also performed to obtain the optimized thicknesses of the individual FM and NM layers in their bi-layer combinations on which, further experiments were conducted for the determination of optical damage threshold. The THz power from these sources grows nearly linearly with the excitation power before the optical damage of the material heterostructure takes place. It has been found that Fe/Ta on the quartz substrate has the highest optical damage threshold of ~85 GW/cm^2. From the many spintronic systems studied here, it was realized that the mean value of the optical damage threshold for such spintronic THz emitters is about 50 GW/cm^2. These results are highly encouraging and suggest that suitable materials and their heterostructures, which provide simultaneously, high optical damage threshold and high THz generation efficiency, can be discovered.

Limitations of the study

The FM and NM layers can be used in various possibilities to form spintronic heterostructures for efficient THz generation. In the current paper, the most popular ones have been studied. The interfacial quality of the

heterostructures needs detailed investigations for enhancing the performance and determining the optical damage at various relevant excitation wavelengths.

FIGURE TITLES AND LEGENDS

Figure 1. THz pulse generation from femtosecond NIR (800 nm) pulse irradiated FM/NM bilayer-type spintronic emitters deposited on quartz substrates at the excitation pulse energy (fluence) of ~0.35 mJ (1.2 mJ/cm^2)

(A) Schematic of the optical pulse excitation and THz pulse generation. B_{ext} is the external magnetic field, J_s is spin current and J_c is charge current density.

(B) Typical time-domain THz signal, E(t) detected by electro-optic sampling.

(C) The Fourier transformed spectrum, E(ω).

(D-I) THz signals from Fe/Pt heterostructures for various combinations of thicknesses (nm) of the Fe and Pt layers.

(J-L) THz signals from CoFeB/Pt and CoFeB/Ta bilayers for various thickness combinations of the two layers.

Figure 2. THz generation from FM/NM bilayers heterostructures and their indiviual constituents

(A) THz signal generated from individual FM and NM layers. A very thin Ta layer (thickness ~1.5 nm) was used as the capping layer for the FM film on quartz substrate.

(B) The THz signal from Fe/Ta bilayers to obtain the optimized thickness of the Fe and Ta layers. Inset: The RMS amplitude of the THz field varying with the increasing thickness of the Ta layer at a fixed thicknesses of the Fe layer (2 nm and 3 nm).

Figure 3. Excitation pulse helicity-dependent THz emission from Fe(2)/Pt(3) bilayer heterostructure

(A) Schematic of the experiment.

(B) Excitation polarization dependent THz time-domain signals.

LP: Linear polarization, LCP: Left-handed circular polarization, RCP: Right-handed circular polarization, EP: Elliptical polarization.

Figure 4. THz generation from FM/NM spintronic emitters in the presence of external magnetic field varying from 0B to 2B

(A) Time-domain THz traces from Fe(2)/Pt(3). Inset: Comparison between applied and no applied magnetic fields. The signal for 0B has been magnified by 4 times.

(B) Time-domain THz traces from Fe(2)/Ta(3). Inset: polarity reversal of the THz signal by reversing the magnetic field direction as per the ISHE in Eq. (1).

Figure 5. THz signal comparison and estimated spin Hall angle values from the THz signal comparison of FM/NM spintronic emitters.

(A) Comparison of the magnitude of the THz signals from Fe/Pt and Fe/Ta with that from the CoFeB/Pt and CoFeB/Ta bilayer heterostructures.

(B) Estimation of spin-Hall angle, γ in α-phase Ta of the Fe(3)/Ta(3) bilayer heterostructure from the comparison between the THz signals from Fe/Pt and Fe/Ta.

Figure 6. Comparison of THz emission efficiency from dual-color air-plasma source to that of spintronic emitter under same excitation power (or pulse energy) and other optical conditions

(A) Comparison between the magnitudes of the time-domain THz traces from dual-color air-plasma source and thickness optimized Fe/Pt spintronic emitter.

(B) Amplitudes of the THz signals from the air-plasma source (blue squares) and the spintronic source (blue spheres) for various excitation pulse energies in our experiments. The graph for THz electric field in kV/cm (red stars) for an air-plasma source is drawn from Ref. [Bartel *et al*.,2005], for a comparison.

Figure 7. Optical damage threshold of various spintronic emitters

(A) Peak THz amplitude with the increasing excitation fluence for the THz emission from a thickness optimized FM/NM spintronic heterostructure. The dashed line in the shaded region indicates the optical damage threshold value. Insets: Optical microscopy images of the sample before and after the damage.

(B) Damage threshold fluence and corresponding damage threshold peak intensity of various spintronic emitters on different substrates under the normal incidence. The numbers inside small parentheses in the names of the sample indicate optimized thickness in nm. Qz: Quartz; Sp: Sapphire; Hs: Highly resistive silicon.

Figure 8. Optical transmittance (T) and reflectance (R) measurements with respect to the incident laser excitation-fluence (average power)

(A) For CoFeB(3)/Pt(3) sample.

(B) For CoFeB(3)/Ta(3) sample.

Solid symbols are for increasing fluences and open symbols are for lowering fluences. Continuous and dotted thin black curves represent the absorptance values. Insets: Optical microscopy images after irradiation of the samples with excitation fluence at the optical damage threshold value indicated by the upward red arrows in the two cases.

STAR★METHODS

RESOURCES AVAILABILITY

Lead contact

Further information and requests for resources should be directed to and will be fulfilled by the lead contact, Prof. Sunil Kumar (kumarsunil@physics.iitd.ac.in)

Material availability

This study did not generate new unique reagents.

Data and code availability

There is no dataset or code associated with this work.

METHOD DETAILS

Sample Preparation and characterization

High-quality bilayer and tri-layer heterostructures of thin films containing ferromagnetic (FM) and nonmagnetic (NM) metallic materials were developed using radio frequency (RF) magnetron sputtering (AJA international). The lateral size of the films was larger than 10 mm x 10 mm and they were deposited on different substrates, 1 mm quartz, 1 mm sapphire, and 0.38 mm highly resistive silicon. The base pressure for the thin film growth was kept at 5×10^{-8} Torr, while the working pressure was kept in the range of 2-5 mTorr according to the optimization condition for each of the deposited material films. Prior to deposition, the substrates were cleaned by double sonication in acetone + isopropyl alcohol (IPA) to remove the contamination from their surfaces. To achieve high purity samples, we used high purity targets and pre-sputtered them to get rid of the impurities on the target

surfaces before the desired film deposition. To ensure good uniformity, the substrate holder was kept rotating at a constant speed during the deposition. Different thickness combinations in the bilayer FM/NM and tri-layer $NM_1/FM/NM_2$ heterostructures were created using Fe and $Co_{20}Fe_{60}B_{20}$ (CoFeB) as ferromagnetic materials and platinum (Pt) and α-phase tantalum (Ta) as nonmagnetic materials at a growth rate of 0.09 Å/sec, 0.25 Å/sec, 0.44 Å/sec, and 0.76 Å/sec, respectively. The RF power was also kept according to the optimized phase of the deposited material, i.e., 150 Watts for Ta and 100Watts for Fe, CoFeB, and Pt. The samples or the substrates were not treated with any pre- and/or post-annealing processes.

The structural and magnetic characterizations of the deposited thin film samples were obtained from X-ray diffraction (XRD), and magnetic hysteresis (M-H) measurements, respectively (see Section S1 of the Supplementary Information). The XRD results confirm the polycrystalline phase of Pt and α-phase of Ta. The surface and interfacial roughness from the XRR fitting were found to be <0.5 nm for all the samples. The in-plane magnetization of the Fe and CoFeB films in Fe/Pt and CoFeB/Pt bilayer heterostructures is confirmed by performing in-plane and out-of-plane M-H measurements. A clear square hysteresis loop with the saturation magnetic field value of <50 Oersted (Coercive field) is obtained for the magnetic layers. Therefore, the samples were kept magnetized along a certain direction by using an external magnetic field value of >50 Oe during the THz generation from the spintronic heterostructures.

THz time-domain spectroscopy

A time-domain THz spectrometer (TDTS) was developed around a Ti:sapphire regenerative amplifier, operating at 1 kHz pulse repetition rate and providing <50 fs laser pulses centered at 800 nm. Dispersion uncompensated pulses were used and the pulse duration at the sample point was ~100 fs. The layout and other details of the setup in different configurations of the measurements are provided in Figure S2.1, S2.2, and S3 of the Supplementary Information. The detection of the THz pulses was made on a [110] oriented 500-micron thick ZnTe crystal by electro-optic sampling. Collimated excitation beam (size ~6 mm) at fixed pulse energy (fluence) of ~0.35 mJ (1.2 mJ/cm^2) was used to irradiate the spintronic emitters in configuration 1 of the setup for determining the optical thickness of the FM and NM layers and their combinations in the heterostructures for best THz power generation efficiency. For quantification of the THz power from the spintronic emitters, we developed a dual-color air plasma-based THz source (see Figure S2.2 of the Supplementary Information). The excitation pulse energy-dependent THz output of our air-plasma source was compared with that from the literature for a similar setup and optical conditions with the excitation pulse and detection. For determining the

optical damage threshold of the spintronic emitters, we used the same experimental setup in configuration 3 as shown in Figure S3. Here, a converging excitation beam passing through the aperture of one of the parabolic mirrors is used for optical pumping of the source, and excitation power was controlled by using a neutral density filter. All the experiments, either with a fixed excitation fluence or with varying fluence, have been performed under the same experimental conditions with the room temperature, humidity (~50%), excitation pulse duration, optical alignment, detection, etc. Therefore, comparisons among different experiments for relative performance parameter was possible.

ACKNOWLEDGMENTS

SK acknowledges the Science and Engineering Research Board (SERB), Department of Science and Technology, Government of India, for financial support through project no. CRG/2020/000892. Joint Advanced Technology Center, IIT Delhi, and Director, LASTEC Delhi are also acknowledged for support through EMDTERA#5 project. Mr. Akash Kumar and Dr. P.K. Muduli are thanked for their help during the material synthesis using UHV sputtering. One of the authors (Sandeep Kumar) acknowledges the University Grants Commission, Government of India for Senior Research Fellowship.

AUTHOR CONTRIBUTIONS

Sunil Kumar supervised the work. Sandeep Kumar performed the experiments. Sunil Kumar and Sandeep Kumar analysed the data and wrote the manuscript. All the authors contributed in finalizing the manuscript.

DECLARATION OF INTERESTS

The authors declare no competing interests.

SUPPLEMENTAL INFORMATION

Supplemental Information can be found online.

REFERENCES

Augst S, Meyerhofer D D, Strickland D and Chin S L 1991 Laser ionization of noble gases by Coulomb-barrier suppression *J. Opt. Soc. Am. B* **8** 858-67

Bansal R, Behera N, Kumar A and Muduli P K 2017 Crystalline phase dependent spin current efficiency in sputtered Ta thin films *Applied Physics Letters* **110** 202402

Bartel T, Gaal P, Reimann K, Woerner M and Elsaesser T 2005 Generation of single-cycle THz transients with high electric-field amplitudes *Opt. Lett.* **30** 2805-7

Battiato M, Carva K and Oppeneer P M 2010 Superdiffusive Spin Transport as a Mechanism of Ultrafast Demagnetization *Physical Review Letters* **105** 027203

Battiato M, Carva K and Oppeneer P M 2012 Theory of laser-induced ultrafast superdiffusive spin transport in layered heterostructures *Physical Review B* **86** 024404

Beaurepaire E, Merle J C, Daunois A and Bigot J Y 1996 Ultrafast Spin Dynamics in Ferromagnetic Nickel *Physical Review Letters* **76** 4250-3

Beaurepaire E, Turner G M, Harrel S M, Beard M C, Bigot J Y and Schmuttenmaer C A 2004 Coherent terahertz emission from ferromagnetic films excited by femtosecond laser pulses *Applied Physics Letters* **84** 3465-7

Chen X, Wu X, Shan S, Guo F, Kong D, Wang C, Nie T, Pandey C, Wen L, Zhao W, Ruan C, Miao J, Li Y and Wang L 2019 Generation and manipulation of chiral broadband terahertz waves from cascade spintronic terahertz emitters *Applied Physics Letters* **115** 221104

Conca A, Heinz B, Schweizer M R, Keller S, Papaioannou E T and Hillebrands B 2017 Lack of correlation between the spin-mixing conductance and the inverse spin Hall effect generated voltages in CoFeB/Pt and CoFeB/Ta bilayers *Physical Review B* **95** 174426

Conca A, Keller S, Mihalceanu L, Kehagias T, Dimitrakopulos G P, Hillebrands B and Papaioannou E T 2016 Study of fully epitaxial Fe/Pt bilayers for spin pumping by ferromagnetic resonance spectroscopy *Physical Review B* **93** 134405

Dang T H, Hawecker J, Rongione E, Baez Flores G, To D Q, Rojas-Sanchez J C, Nong H, Mangeney J, Tignon J, Godel F, Collin S, Seneor P, Bibes M, Fert A, Anane M, George J M, Vila L, Cosset-Cheneau M, Dolfi D, Lebrun R, Bortolotti P, Belashchenko K, Dhillon S and Jaffrès H 2020 Ultrafast spin-currents and charge conversion at 3d-5d interfaces probed by time-domain terahertz spectroscopy *Applied Physics Reviews* **7** 041409

Feng Z, Yu R, Zhou Y, Lu H, Tan W, Deng H, Liu Q, Zhai Z, Zhu L, Cai J, Miao B and Ding H 2018 Highly Efficient Spintronic Terahertz Emitter Enabled by Metal–Dielectric Photonic Crystal *Advanced Optical Materials* **6** 1800965

Fülöp J A, Pálfalvi L, Almási G and Hebling J 2010 Design of high-energy terahertz sources based on optical rectification *Opt. Express* **18** 12311-27

Fülöp J A, Tzortzakis S and Kampfrath T 2020 Laser-Driven Strong-Field Terahertz Sources *Advanced Optical Materials* **8** 1900681

Gallot G and Grischkowsky D 1999 Electro-optic detection of terahertz radiation *J. Opt. Soc. Am. B* **16** 1204-12

Haney P M, Lee H-W, Lee K-J, Manchon A and Stiles M D 2013 Current induced torques and interfacial spin-orbit coupling: Semiclassical modeling *Physical Review B* **87** 174411

Hauri C P, Ruchert C, Vicario C and Ardana F 2011 Strong-field single-cycle THz pulses generated in an organic crystal *Applied Physics Letters* **99** 161116

Herapath R I, Hornett S M, Seifert T S, Jakob G, Kläui M, Bertolotti J, Kampfrath T and Hendry E 2019 Impact of pump wavelength on terahertz emission of a cavity-enhanced spintronic trilayer *Applied Physics Letters* **114** 041107

Hilton D J, Averitt R D, Meserole C A, Fisher G L, Funk D J, Thompson J D and Taylor A J 2004 Terahertz emission via ultrashort-pulse excitation of magnetic metalfilms *Opt. Lett.* **29** 1805-7

Hoffmann A 2013 Spin Hall Effects in Metals *IEEE Transactions on Magnetics* **49** 5172-93

Huang L, Kim J-W, Lee S-H, Kim S-D, Tien V M, Shinde K P, Shim J-H, Shin Y, Shin H J, Kim S, Park J, Park S-Y, Choi Y S, Kim H-J, Hong J-I, Kim D E and Kim D-H 2019 Direct observation of terahertz emission from ultrafast spin dynamics in thick ferromagnetic films *Applied Physics Letters* **115** 142404

Huang L, Lee S-H, Kim S-D, Shim J-H, Shin H J, Kim S, Park J, Park S-Y, Choi Y S, Kim H-J, Hong J-I, Kim D E and Kim D-H 2020 Universal field-tunable terahertz emission by ultrafast photoinduced demagnetization in Fe, Ni, and Co ferromagnetic films *Scientific Reports* **10** 15843

Huisman T J, Mikhaylovskiy R V, Costa J D, Freimuth F, Paz E, Ventura J, Freitas P P, Blügel S, Mokrousov Y, Rasing T and Kimel A V 2016 Femtosecond control of electric currents in metallic ferromagnetic heterostructures *Nature Nanotechnology* **11** 455-8

Kadlec F, Kužel P and Coutaz J-L 2004 Optical rectification at metal surfaces *Opt. Lett.* **29** 2674-6

Kampfrath T, Battiato M, Maldonado P, Eilers G, Nötzold J, Mährlein S, Zbarsky V, Freimuth F, Mokrousov Y, Blügel S, Wolf M, Radu I, Oppeneer P M and Münzenberg M 2013a Terahertz spin current pulses controlled by magnetic heterostructures *Nature Nanotechnology* **8** 256

Kampfrath T, Tanaka K and Nelson K A 2013b Resonant and nonresonant control over matter and light by intense terahertz transients *Nature Photonics* **7** 680-90

Kim D-J, Kim S-I, Park S-Y, Lee K-D and Park B-G 2014 Ferromagnetic resonance spin pumping in CoFeB with highly resistive non-magnetic electrodes *Current Applied Physics* **14** 1344-8

Kim S-I, Kim D-J, Seo M-S, Park B-G and Park S-Y 2015 Dependence of inverse-spin Hall effect and spin-rectified voltage on tantalum thickness in Ta/CoFeB bilayer structure *Applied Physics Letters* **106** 032409

Knorren R, Bennemann K H, Burgermeister R and Aeschlimann M 2000 Dynamics of excited electrons in copper and ferromagnetic transition metals: Theory and experiment *Physical Review B* **61** 9427-40

Kong D, Wu X, Wang B, Nie T, Xiao M, Pandey C, Gao Y, Wen L, Zhao W, Ruan C, Miao J, Li Y and Wang L 2019 Broadband Spintronic Terahertz Emitter with Magnetic-Field Manipulated Polarizations *Advanced Optical Materials* **7** 1900487

Kress M, Löffler T, Eden S, Thomson M and Roskos H G 2004 Terahertz-pulse generation by photoionization of air with laser pulses composed of both fundamental and second-harmonic waves *Opt. Lett.* **29** 1120-2

Kumar A, Bansal R, Chaudhary S and Muduli P K 2018 Large spin current generation by the spin Hall effect in mixed crystalline phase Ta thin films *Physical Review B* **98** 104403

Kumar N, Hendrikx R W A, Adam A J L and Planken P C M 2015 Thickness dependent terahertz emission from cobalt thin films *Opt. Express* **23** 14252-62

Kumar S, Nivedan A, Singh A and Kumar S 2021a THz pulses from optically excited Fe-, Pt- and Ta-based spintronic heterostructures *Pramana* **95** 75

Kumar S, Singh A, Kumar S, Nivedan A, Tondusson M, Degert J, Oberlé J, Yun S J, Lee Y H and Freysz E 2021b Enhancement in optically induced ultrafast THz response of MoSe2MoS2 heterobilayer *Opt. Express* **29** 4181-90

Kumar S, Singh A, Nivedan A, Kumar S, Yun S J, Lee Y H, Tondusson M, Degert J, Oberle J and Freysz E 2021c Sub-bandgap activated charges transfer in a graphene-MoS2-graphene heterostructure *Nano Select* **1**

Li G, Medapalli R, Mikhaylovskiy R V, Spada F E, Rasing T, Fullerton E E and Kimel A V 2019 THz emission from Co/Pt bilayers with varied roughness, crystal structure, and interface intermixing *Physical Review Materials* **3** 084415

Liu L, Pai C-F, Li Y, Tseng H, Ralph D and Buhrman R J S 2012 Spin-torque switching with the giant spin Hall effect of tantalum **336** 555-8

Melnikov A, Razdolski I, Wehling T O, Papaioannou E T, Roddatis V, Fumagalli P, Aktsipetrov O, Lichtenstein A I and Bovensiepen U 2011 Ultrafast Transport of Laser-Excited Spin-Polarized Carriers in Au/Fe/MgO (001) *Physical Review Letters* **107** 076601

Meng Q, Zhang B, Zhong S and Zhu L 2016 Damage threshold of lithium niobate crystal under single and multiple femtosecond laser pulses: theoretical and experimental study *Applied Physics A* **122** 582

Mondal S, Choudhury S, Jha N, Ganguly A, Sinha J and Barman A 2017 All-optical detection of the spin Hall angle in W/CoFeB/SiO2 heterostructures with varying thickness of the tungsten layer *Physical Review B* **96** 054414

Mosendz O, Pearson J E, Fradin F Y, Bauer G E W, Bader S D and Hoffmann A 2010 Quantifying Spin Hall Angles from Spin Pumping: Experiments and Theory *Physical Review Letters* **104** 046601

Niimi Y and Otani Y 2015 Reciprocal spin Hall effects in conductors with strong spin–orbit coupling: a review *Reports on Progress in Physics* **78** 124501

Obstbaum M, Härtinger M, Bauer H G, Meier T, Swientek F, Back C H and Woltersdorf G 2014 Inverse spin Hall effect in Ni81Fe19/normal-metal bilayers *Physical Review B* **89** 060407

Oh T I, Yoo Y J, You Y S and Kim K Y 2014 Generation of strong terahertz fields exceeding 8 MV/cm at 1 kHz and real-time beam profiling *Applied Physics Letters* **105** 041103

Papaioannou E T and Beigang R 2021 THz spintronic emitters: a review on achievements and future challenges *Nanophotonics* **10** 1243-57

Papaioannou E T, Fuhrmann P, Jungfleisch M B, Brächer T, Pirro P, Lauer V, Lösch J and Hillebrands B 2013 Optimizing the spin-pumping induced inverse spin Hall voltage by crystal growth in Fe/Pt bilayers *Applied Physics Letters* **103** 162401

Qiu H, Zhou L, Zhang C, Wu J, Tian Y, Cheng S, Mi S, Zhao H, Zhang Q, Wu D, Jin B, Chen J and Wu P 2020 Ultrafast spin current generated from an antiferromagnet *Nature Physics*

Qiu H S, Kato K, Hirota K, Sarukura N, Yoshimura M and Nakajima M 2018 Layer thickness dependence of the terahertz emission based on spin current in ferromagnetic heterostructures *Opt. Express* **26** 15247-54

Saitoh E, Ueda M, Miyajima H and Tatara G 2006 Conversion of spin current into charge current at room temperature: Inverse spin-Hall effect *Applied Physics Letters* **88** 182509

Seifert T, Jaiswal S, Martens U, Hannegan J, Braun L, Maldonado P, Freimuth F, Kronenberg A, Henrizi J, Radu I, Beaurepaire E, Mokrousov Y, Oppeneer P M, Jourdan M, Jakob G, Turchinovich D, Hayden L M, Wolf M, Münzenberg M, Kläui M and Kampfrath T 2016 Efficient metallic spintronic emitters of ultrabroadband terahertz radiation *Nature Photonics* **10** 483

Seifert T, Jaiswal S, Sajadi M, Jakob G, Winnerl S, Wolf M, Kläui M and Kampfrath T 2017a Ultrabroadband single-cycle terahertz pulses with peak fields of 300 kV cm−1 from a metallic spintronic emitter *Applied Physics Letters* **110** 252402

Seifert T, Martens U, Günther S, Schoen M A W, Radu F, Chen X Z, Lucas I, Ramos R, Aguirre M H, Algarabel P A, Anadón A, Körner H S, Walowski J, Back C, Ibarra M R, Morellón L, Saitoh E, Wolf M, Song C, Uchida K, Münzenberg M, Radu I and Kampfrath T 2017b Terahertz Spin Currents and Inverse Spin Hall Effect in Thin-Film Heterostructures Containing Complex Magnetic Compounds *SPIN* **07** 1740010

Seifert T S, Tran N M, Gueckstock O, Rouzegar S M, Nadvornik L, Jaiswal S, Jakob G, Temnov V V, Münzenberg M, Wolf M, Kläui M and Kampfrath T 2018 Terahertz spectroscopy for all-optical spintronic characterization of the spin-Hall-effect metals Pt, W and Cu80Ir20 *Journal of Physics D: Applied Physics* **51** 364003

Seki T, Hasegawa Y, Mitani S, Takahashi S, Imamura H, Maekawa S, Nitta J and Takanashi K 2008 Giant spin Hall effect in perpendicularly spin-polarized FePt/Au devices *Nature Materials* **7** 125-9

Sinova J, Valenzuela S O, Wunderlich J, Back C H and Jungwirth T 2015 Spin Hall effects *Reviews of Modern Physics* **87** 1213-60

Torosyan G, Keller S, Scheuer L, Beigang R and Papaioannou E T 2018 Optimized Spintronic Terahertz Emitters Based on Epitaxial Grown Fe/Pt Layer Structures *Scientific Reports* **8** 1311

Wu Y, Elyasi M, Qiu X, Chen M, Liu Y, Ke L and Yang H 2017 High-Performance THz Emitters Based on Ferromagnetic/Nonmagnetic Heterostructures *Advanced Materials* **29** 1603031

Xin X, Altan H, Saint A, Matten D and Alfano R R 2006 Terahertz absorption spectrum of para and ortho water vapors at different humidities at room temperature *Journal of Applied Physics* **100** 094905

Yang D, Liang J, Zhou C, Sun L, Zheng R, Luo S, Wu Y and Qi J 2016 Powerful and Tunable THz Emitters Based on the Fe/Pt Magnetic Heterostructure *Advanced Optical Materials* **4** 1944-9

Zhang Q, Luo Z, Li H, Yang Y, Zhang X and Wu Y 2019 Terahertz Emission from Anomalous Hall Effect in a Single-Layer Ferromagnet *Physical Review Applied* **12** 054027

Zhu L, Ralph D C and Buhrman R A 2019 Effective Spin-Mixing Conductance of Heavy-Metal--Ferromagnet Interfaces *Physical Review Letters* **123** 057203

Figure 1

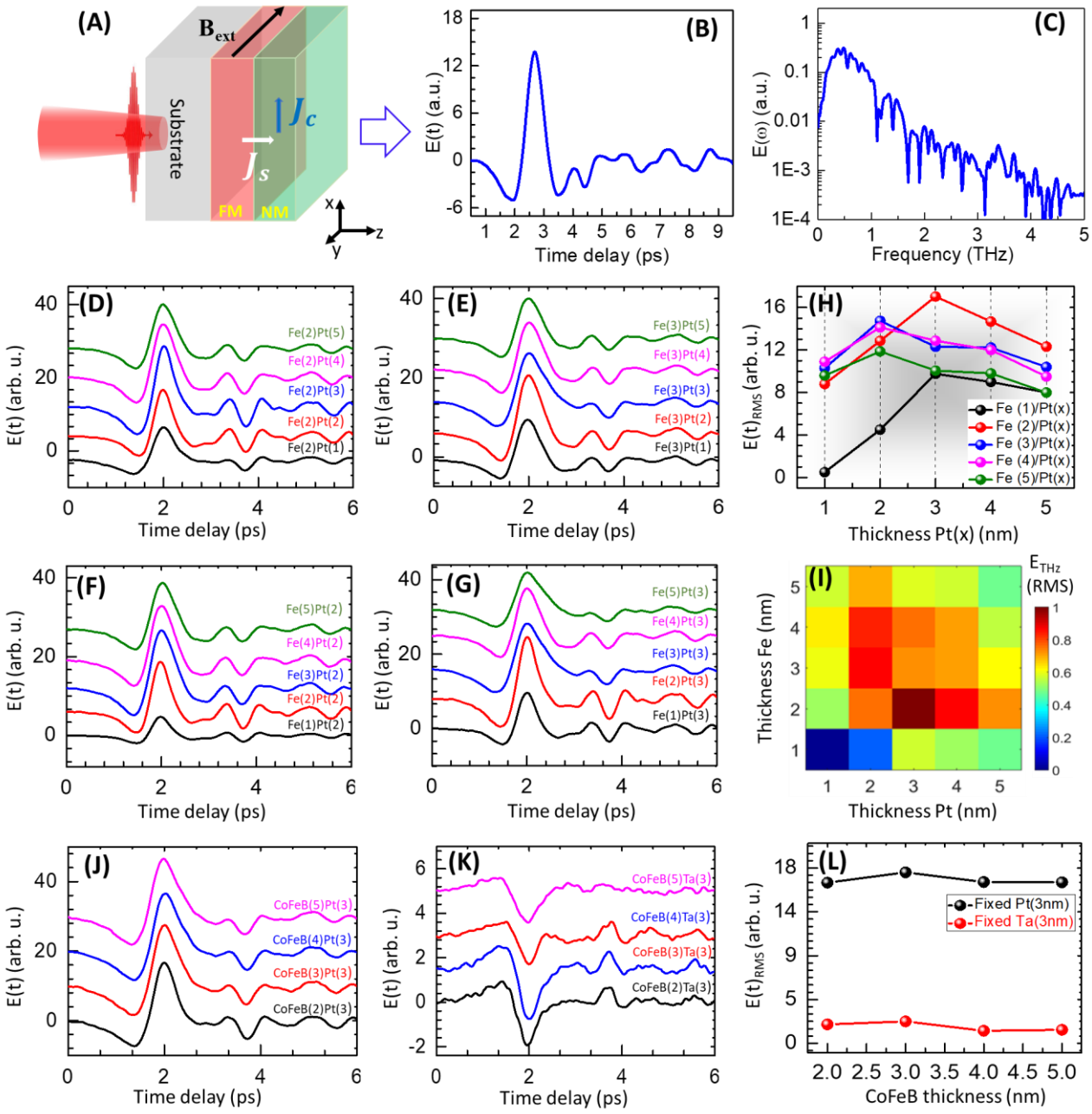
(A)
B_ext
Substrate
J_c
J_s
FM
NM
x
z
y
(B)
E(t) (a.u.)
Time delay (ps)
(C)
E(ω) (a.u.)
Frequency (THz)
(D)
E(t) (arb. u.)
Fe(2)Pt(5)
Fe(2)Pt(4)
Fe(2)Pt(3)
Fe(2)Pt(2)
Fe(2)Pt(1)
Time delay (ps)
(E)
Fe(3)Pt(5)
Fe(3)Pt(4)
Fe(3)Pt(3)
Fe(3)Pt(2)
Fe(3)Pt(1)
Time delay (ps)
(H)
E(t)_RMS (arb. u.)
Fe (1)/Pt(x)
Fe (2)/Pt(x)
Fe (3)/Pt(x)
Fe (4)/Pt(x)
Fe (5)/Pt(x)
Thickness Pt(x) (nm)
(F)
E(t) (arb. u.)
Fe(5)Pt(2)
Fe(4)Pt(2)
Fe(3)Pt(2)
Fe(2)Pt(2)
Fe(1)Pt(2)
Time delay (ps)
(G)
Fe(5)Pt(3)
Fe(4)Pt(3)
Fe(3)Pt(3)
Fe(2)Pt(3)
Fe(1)Pt(3)
Time delay (ps)
(I)
E_THz (RMS)
Thickness Fe (nm)
Thickness Pt (nm)
(J)
E(t) (arb. u.)
CoFeB(5)Pt(3)
CoFeB(4)Pt(3)
CoFeB(3)Pt(3)
CoFeB(2)Pt(3)
Time delay (ps)
(K)
E(t) (arb. u.)
CoFeB(5)Ta(3)
CoFeB(4)Ta(3)
CoFeB(3)Ta(3)
CoFeB(2)Ta(3)
Time delay (ps)
(L)
E(t)_RMS (arb. u.)
Fixed Pt(3nm)
Fixed Ta(3nm)
CoFeB thickness (nm)

Figure 2

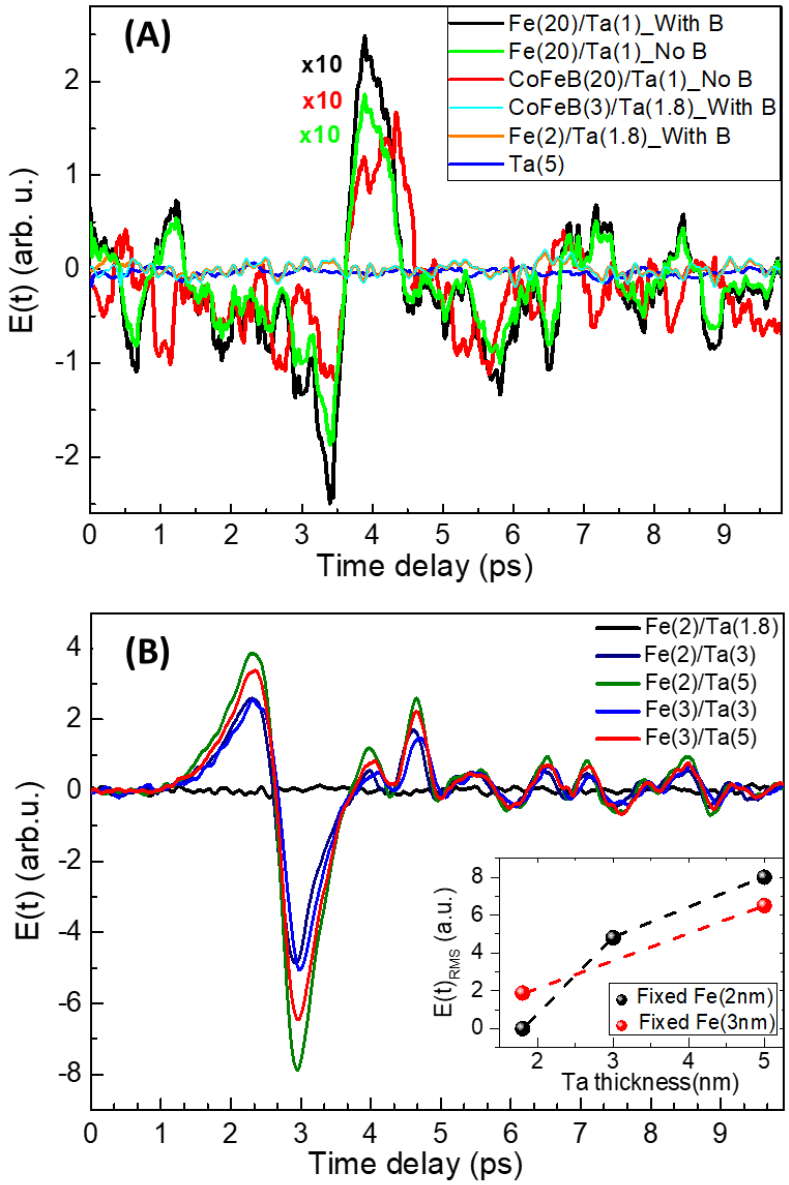
(A)
x10
x10
x10
Fe(20)/Ta(1)_With B
Fe(20)/Ta(1)_No B
CoFeB(20)/Ta(1)_No B
CoFeB(3)/Ta(1.8)_With B
Fe(2)/Ta(1.8)_With B
Ta(5)
E(t) (arb. u.)
Time delay (ps)
(B)
Fe(2)/Ta(1.8)
Fe(2)/Ta(3)
Fe(2)/Ta(5)
Fe(3)/Ta(3)
Fe(3)/Ta(5)
E(t) (arb.u.)
Time delay (ps)
E(t)RMS (a.u.)
Fixed Fe(2nm)
Fixed Fe(3nm)
Ta thickness(nm)

Figure 3

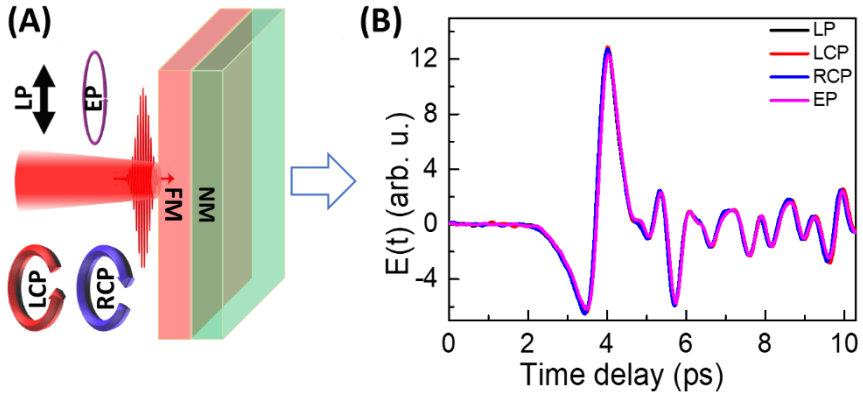
(A)
LP
EP
FM
NM
LCP
RCP
(B)
LP
LCP
RCP
EP
E(t) (arb. u.)
12
8
4
0
-4
0
2
4
6
8
10
Time delay (ps)

Figure 4

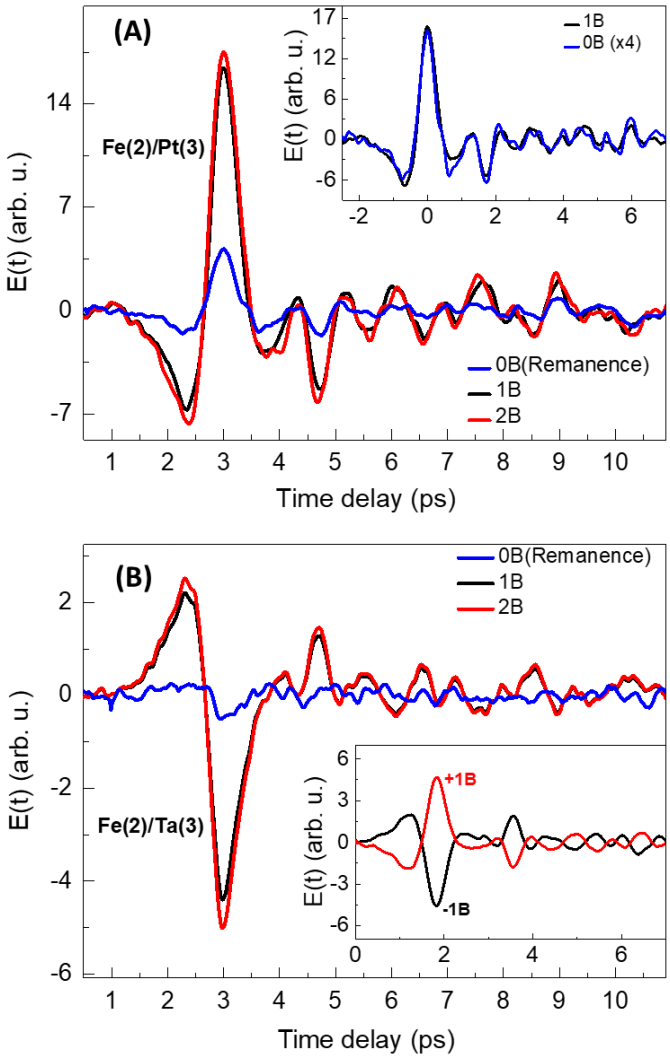
(A)
Fe(2)/Pt(3)
E(t) (arb. u.)
Time delay (ps)
0B(Remanence)
1B
2B
1B
0B (x4)
(B)
Fe(2)/Ta(3)
+1B
-1B

Figure 5

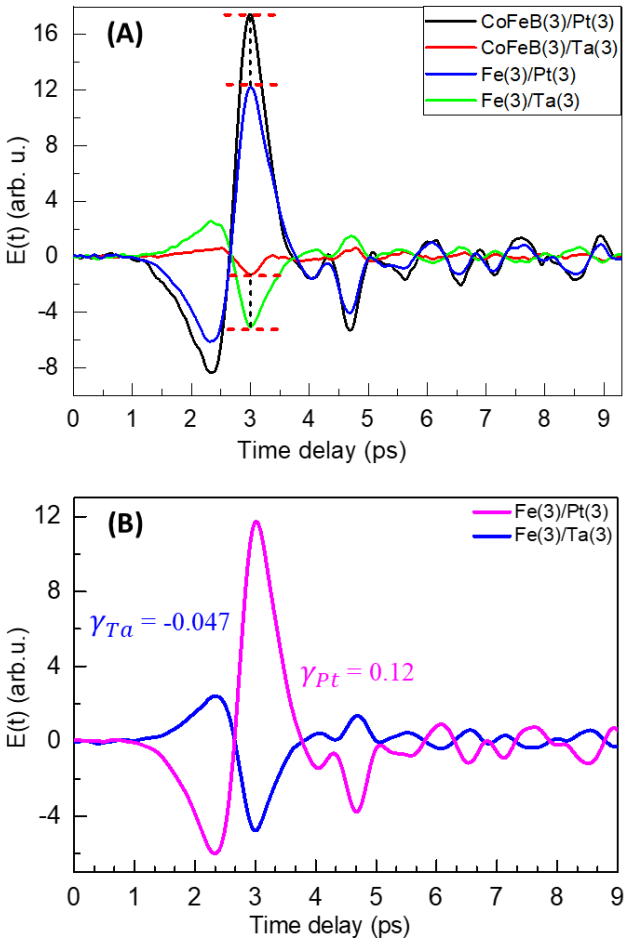
(A)
CoFeB(3)/Pt(3)
CoFeB(3)/Ta(3)
Fe(3)/Pt(3)
Fe(3)/Ta(3)
E(t) (arb. u.)
Time delay (ps)
(B)
Fe(3)/Pt(3)
Fe(3)/Ta(3)
γ_{Ta} = -0.047
γ_{Pt} = 0.12
E(t) (arb.u.)
Time delay (ps)

Figure 6

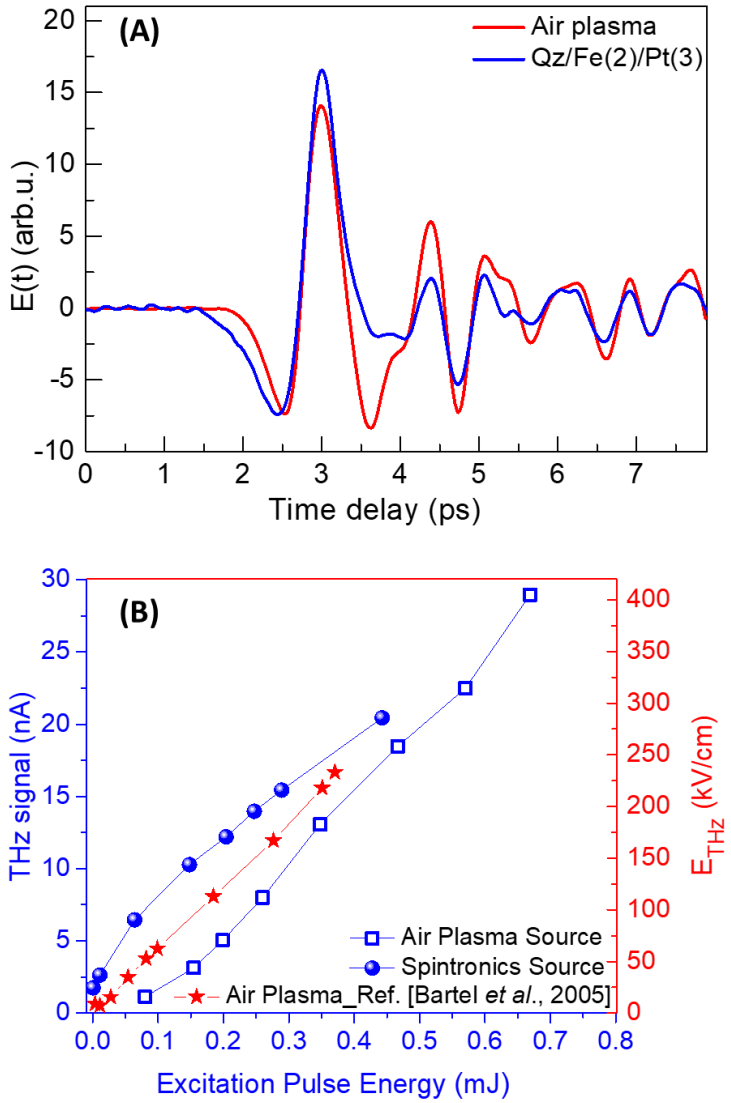
(A)
Air plasma
Qz/Fe(2)/Pt(3)
E(t) (arb.u.)
Time delay (ps)
(B)
THz signal (nA)
E_{THz} (kV/cm)
Air Plasma Source
Spintronics Source
Air Plasma_Ref. [Bartel *et al.*, 2005]
Excitation Pulse Energy (mJ)

Figure 7

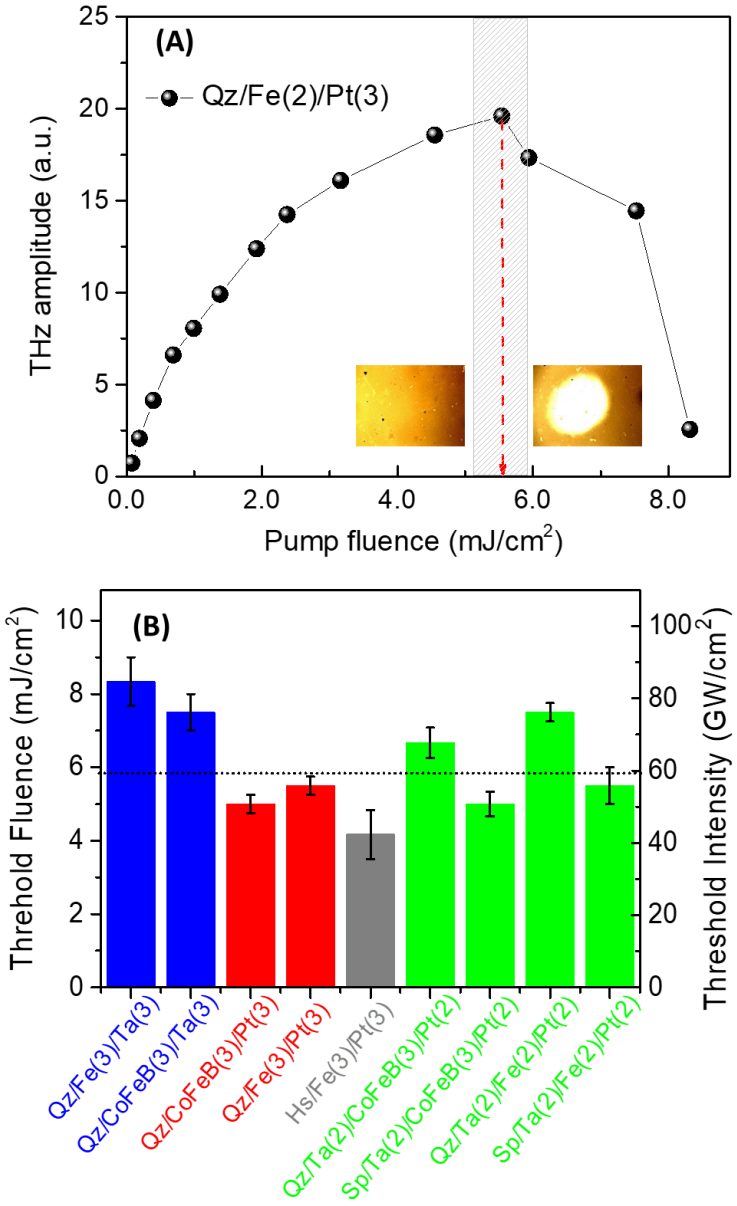
(A)
Qz/Fe(2)/Pt(3)
THz amplitude (a.u.)
Pump fluence (mJ/cm²)
(B)
Threhold Fluence (mJ/cm²)
Threshold Intensity (GW/cm²)
Qz/Fe(3)/Ta(3)
Qz/CoFeB(3)/Ta(3)
Qz/CoFeB(3)/Pt(3)
Qz/Fe(3)/Pt(3)
Hs/Fe(3)/Pt(3)
Qz/Ta(2)/CoFeB(3)/Pt(2)
Sp/Ta(2)/CoFeB(3)/Pt(2)
Qz/Ta(2)/Fe(2)/Pt(2)
Sp/Ta(2)/Fe(2)/Pt(2)

Figure 8

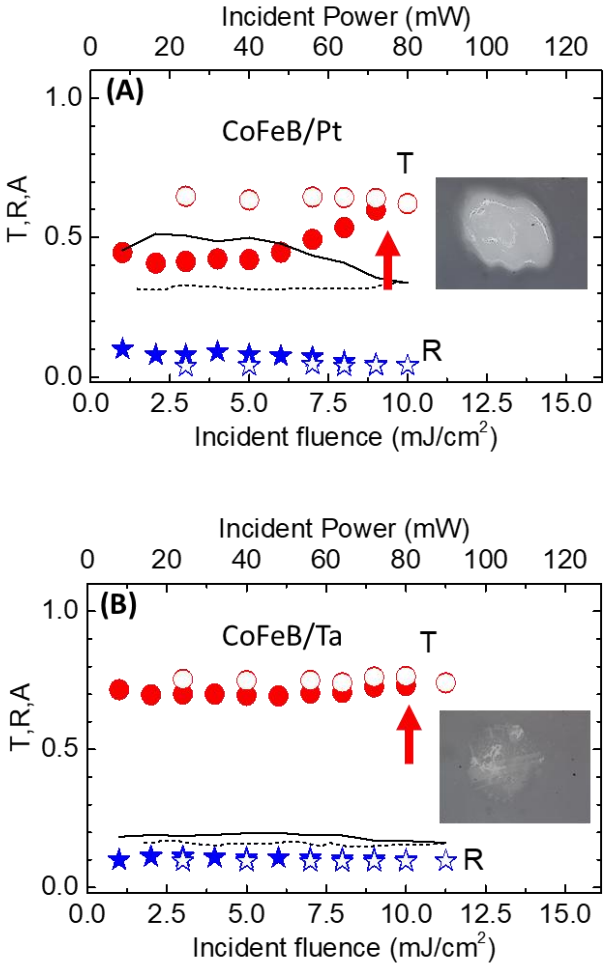
Incident Power (mW)
0 20 40 60 80 100 120
(A)
CoFeB/Pt
T
R
T,R,A
1.0
0.5
0.0
0.0 2.5 5.0 7.5 10.0 12.5 15.0
Incident fluence (mJ/cm2)
Incident Power (mW)
0 20 40 60 80 100 120
(B)
CoFeB/Ta
T
R
T,R,A
1.0
0.5
0.0
0.0 2.5 5.0 7.5 10.0 12.5 15.0
Incident fluence (mJ/cm2)